Journal of
Synchrotron Radiation

ISSN 0909-0495

Received 2 March 2012
Accepted 10 September 2012

QXAFS system of the BL14W1 XAFS beamline at the Shanghai Synchrotron Radiation Facility

Heng Liu, Yongnian Zhou, Zheng Jiang,* Songqi Gu, Xiangjun Wei, Yuying Huang, Yang Zou* and Hongjie Xu*

Shanghai Synchrotron Radiation Facility, Shanghai Institute of Applied Physics, Chinese Academy of Sciences, Zhang Heng Road No. 239, Pu Dong District, PO Box 918, Shanghai 201204, People's Republic of China. E-mail: jiangzheng@sinap.ac.cn, zouyang@sinap.ac.cn, xuhongjie@sianp.ac.cn

The quick-scanning XAFS (QXAFS) method is achieved at the BL14W1 XAFS beamline at the Shanghai Synchrotron Radiation Facility based on the *EPICS* and *LabVIEW* systems. This is realised by the unprecedented use of *LabVIEW*'s data logging and supervisory control module for communication with *EPICS* in synchrotron radiation facilities. A fine QXAFS spectrum with an energy range of 1.2 keV at the Cu *K*-edge has been collected in 2 s with stable beam position and the data quality is comparable with that of the step-mode XAFS spectrum. Analog-to-digital converter and double-crystal monochromator set-ups have been optimized in order to acquire optimal parameters for the QXAFS experiments. Signal-to-noise ratios of these spectra have been calculated in order to estimate the importance of these parameters.

Keywords: QXAFS; beamline; *EPICS*; *LabVIEW*; DSC.

1. Introduction

As a time-resolved method, the QXAFS technique was developed by R. Frahm at HASYLAB in 1987 (Frahm, 1988, 1989). Since then, the QXAFS technique has attracted scientists' attention in the fields of materials and catalysts because of its advantages in short-time scanning (Beale & Sankar, 2006; Cattaneo *et al.*, 2001; Oudenhuijzen *et al.*, 2002) that plays an important role in investigations of quick changes of physical and chemical reactions (Lützenkirchen-Hecht *et al.*, 1996; Newton *et al.*, 2002; Pirngruber *et al.*, 2004; Grandjean *et al.*, 2005). It can also be used to study dilute samples (Hermes *et al.*, 2006) owing to the high-intensity light source. The short measurement time of QXAFS could also significantly reduce radiation damage to samples, which is especially important for biological samples. With the development of mechanics and electronics, the QXAFS technique with a time resolution of milliseconds has been developed, allowing for investigations into very quick reactions (Richwin *et al.*, 2001; Lützenkirchen-Hecht *et al.*, 2001; Caliebe *et al.*, 2006; Uruga *et al.*, 2007; Khalid *et al.*, 2010; Stötzel *et al.*, 2011).

One of the major differences of QXAFS compared with the conventional XAFS method is that the Bragg motor moves continuously and quickly from the beginning to the end. Then typically one spectrum can be acquired at a second level. To this end a much more stabilized mechanical system, especially in terms of the rigid parallelism of the two crystals during the movement of the Bragg motor, is required. Another critical factor for QXAFS is the quick electronics system that permits fast data acquisition.

We have developed the QXAFS technique at high resolution at beamline BL14W1 XAFS of the Shanghai Synchrotron Radiation Facility (SSRF), by using NI (National Instrument) *LabVIEW*'s Data logging and Supervisory Control (DSC) module communication with *EPICS* (*Experimental Physics and Industrial Control System*). To the best of our knowledge we are the first to use this method at synchrotron radiation facilities. This paper describes the essential optics and electronics system. Absorption spectra of Cu foil under different conditions were measured in order to obtain optimal parameters for the QXAFS experiments. Signal-to-noise ratios of these spectra were calculated in order to estimate their quality.

2. X-ray source and beamline

2.1. Beamline layout

BL14W1 is a wiggler beamline. The source of the beamline is a 1.5 m-long 38-pole wiggler with maximum magnetic field strength of 1.2 T. The layout of the beamline is shown in Fig. 1. The main parameters of the beamline are shown in Table 1. The maximum photon flux at 10 keV can reach up to 1×10^{13} photons s^{-1} (0.1% bandwidth)$^{-1}$.

A liquid-nitrogen-cooled (LN) double-crystal monochromator (DCM) is positioned at 25 m from the source point, immediately after a collimation mirror at 22 m from the source. The collimating mirror is set at a grazing incident angle of 2.8 mrad, and reflects upward. A toroidal mirror at 28 m focuses the beam to the sample point at 42 m. Near the sample position a harmonics rejection mirror is used to restrain higher

Table 1
Design parameters of the SSRF BL14W1 beamline.

Equipment	SSRF XAFS
Light source	38-pole wiggler
Electron energy	3.5 GeV
Magnetic field intensity	1.2 T
Beam intensity	300 mA
Beamline acceptance angle	1.0 mrad × 0.14 mrad (H × V)
Energy range	4–22.5 keV, focused 3.5–50 keV, unfocused
Energy resolution ($\Delta E/E$)	1.5×10^{-4} Si(111) at 10 keV 0.5×10^{-4} Si(311) at 10 keV
Time resolution capability	2 s at Cu *K*-edge (8750–9950 eV)
Flux at sample	$>1.0 \times 10^{13}$ photons s^{-1} (0.1% bandwidth)$^{-1}$ at 10 keV Si(111) focused, 300 mA (calculated)
Focused spot size (min)	0.3 mm × 0.3 mm (H × V)
High harmonic content	$<10^{-4}$ harmonic suppression mirror (focused)
Detection model	Transmission, fluorescence, electron yield

harmonics in low-energy experiments. The angle of the harmonics rejection mirror is set to 5 mrad with three different coating layers, Si, Ni and Rh.

2.1.1. Stability of the DCM. A fixed-vertical-offset LN DCM with Si(111) and Si(311) crystals was produced by Bruker (formerly ACCEL). The relation between energy range and flux is shown in Fig. 2. The maximum speed of the Bragg motor was 0.9° s^{-1}. A vertical adjustment machine on the second crystal (T2 stage) was used to fix the vertical offset during the energy scan.

T2 values at different energy are shown in Fig. 3, showing that the differences of the T2 values are small in the energy range of a typical XAFS spectrum (pre-edge 200 eV, post-edge 800 eV, total 1 keV). For example, compensation of the T2 value is about 0.045 mm when the edge energy is ∼10 keV. The parallelity of the two crystals is less than 0.1 µrad both in the horizontal and vertical direction during the scan process. Test results show that the stability of the DCM system is good enough for QXAFS scanning. All of the spectra in this paper were acquired using the T2 correction.

2.2. QXAFS hardware system

Fig. 4 shows a schematic of the QXAFS system. The left-hand part shows the *EPICS* hardware which can be used to control and read data from the DCM system. The right-hand part shows the data acquisition system for sampling.

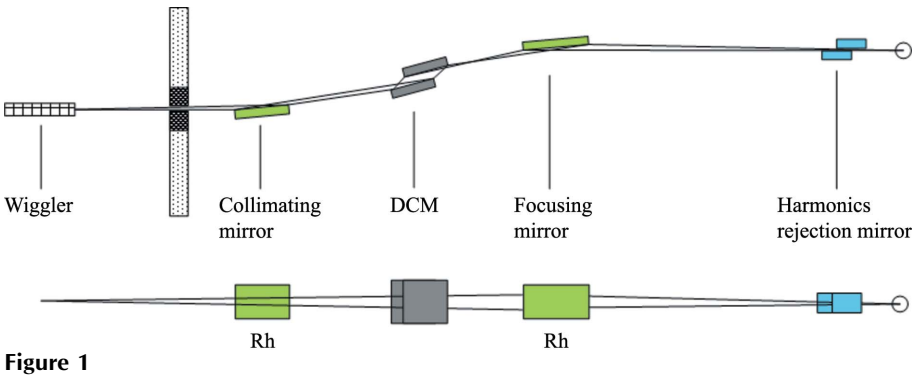

Figure 1
Layout of the BL14W1 XAFS beamline.

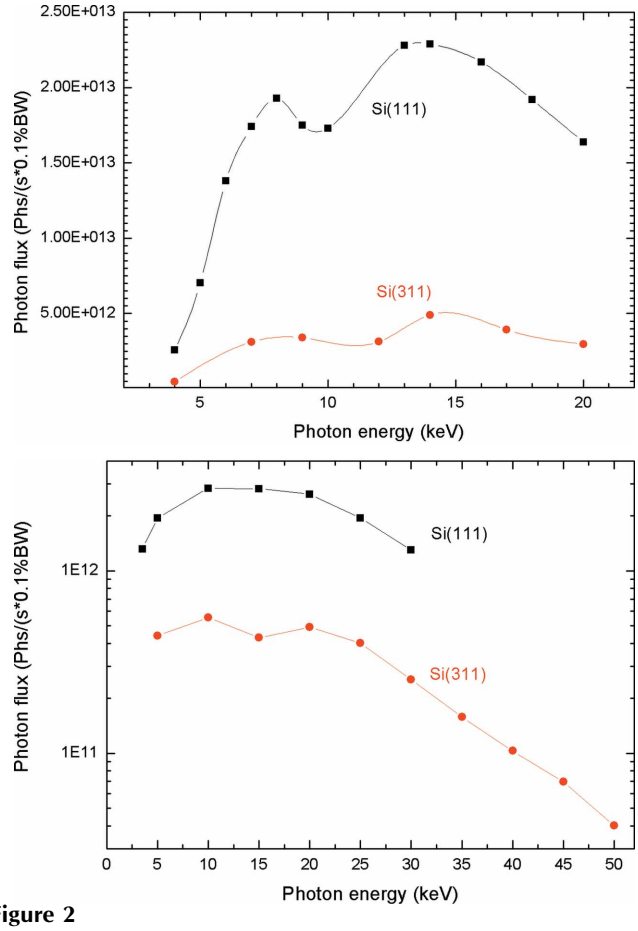

Figure 2
Relation between energy and flux (top, focused; bottom, unfocused).

The *EPICS* system and the *VxWorks* system run on embedded CPU card MVME5500 from the American company Pro-Dex. The eight axes control cards MAXv-8000 from the American company OMS, SLS2017 and SLS2013, are used to translate the signal to control the movement of the DCM motors. When the Bragg motor is moving, the change in angle can be translated to an RGF20F readhead and RGF0400 interface (Renishaw). Then the data are sent back to the OPI PC. By using the hardware above, the *EPICS* system can control and record the movement of the DCM motors.

The sampling system hardware includes three ionization chambers, three low-current amplifiers (DLPCA-200, Femto Company), a computer and an analog-to-digital converter (ADC) (PMC66-16AISS8AO4, GSC Company) card inserted into one PCI slot of the computer. The ionization chambers DIC0100 (Oxford Danfysik Company) are designed to operate at pressures from 0.5 to 2 bar. The currents of the three ionization chambers are amplified by the three low-current amplifiers to voltages, and then sampled simultaneously by the ADC with 16-bit resolution and 2 MHz highest sampling speed. The ADC can work in DMA

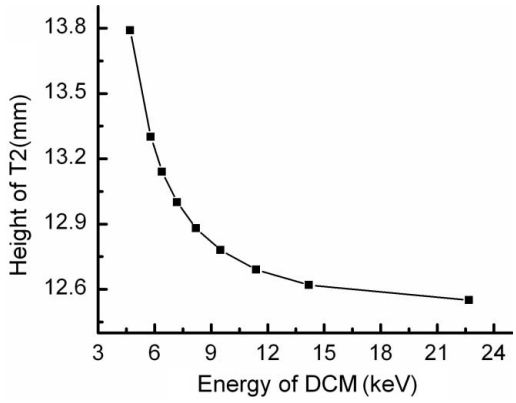

Figure 3
T2 value of the LN DCM at different energies.

(direct memory access) mode and FIFO (first in, first out) mode with a 256 K buffer register.

2.3. QXAFS software system

The *EPICS* system is used to control the DCM system. *EPICS* can provide a standard distributed control system architecture, communication protocol, run-time database and software tools. Furthermore, many I/O devices can be supported by *EPICS*. To date, *EPICS* has been used as a control system at many large physical experimental facilities around the world.

Data acquisition software is written in *LabVIEW*. The advantage of *LabVIEW* is that it has a user-friendly graphical user interface and an easy control model for different types of hardware. It has been used at worldwide synchrotron radiation facilities, especially at XAFS beamlines such as the 1W1B station at the Beijing Synchrotron Radiation Facility (Liu *et al.*, 2004), SRS beamline 9.3 (UK) and the APS PNC-CAT beamline (USA).

Considering the hardware and software architecture, *LabVIEW* communicates with the *EPICS* system *via* the DSC control module.

2.3.1. NI *LabVIEW* DSC module. The control system of BL14W1 is based on the *EPICS* distributed system. With the DSC module, control commands can be sent from the experimental station data acquisition system to the DCM system and the data can be read back. For the architecture of the whole hardware system, the acquisition system of the station has to cooperate with the distributed *EPICS* systems effectively.

Before being used for experimental station data acquisition software, DSC has been widely applied in industrial control systems in recent years (Beck *et al.*, 2006). Therefore, we are trying to extend the usage of the DSC module into the synchrotron research field. The DSC module is used to connect the beamline control system and the data acquisition system at BL14W1 at SSRF.

There are two main advantages of using the DSC module. The first is that it is suitable for the system architecture. Compared with the Shared Memory Interface the DSC module is a good way to organize the system and has a user-friendly graphical user interface for programmers. The second advantage concerns communication time: the original communication time between *EPICS* and *LabVIEW* is too long for the QXAFS method; the time using the Active-X system has up to tens of seconds of delay. In contrast, using the DSC module could reduce the time delay to tens of milliseconds which is acceptable for a second-level QXAFS scan. In order to correct the offset in data analysis, currently a

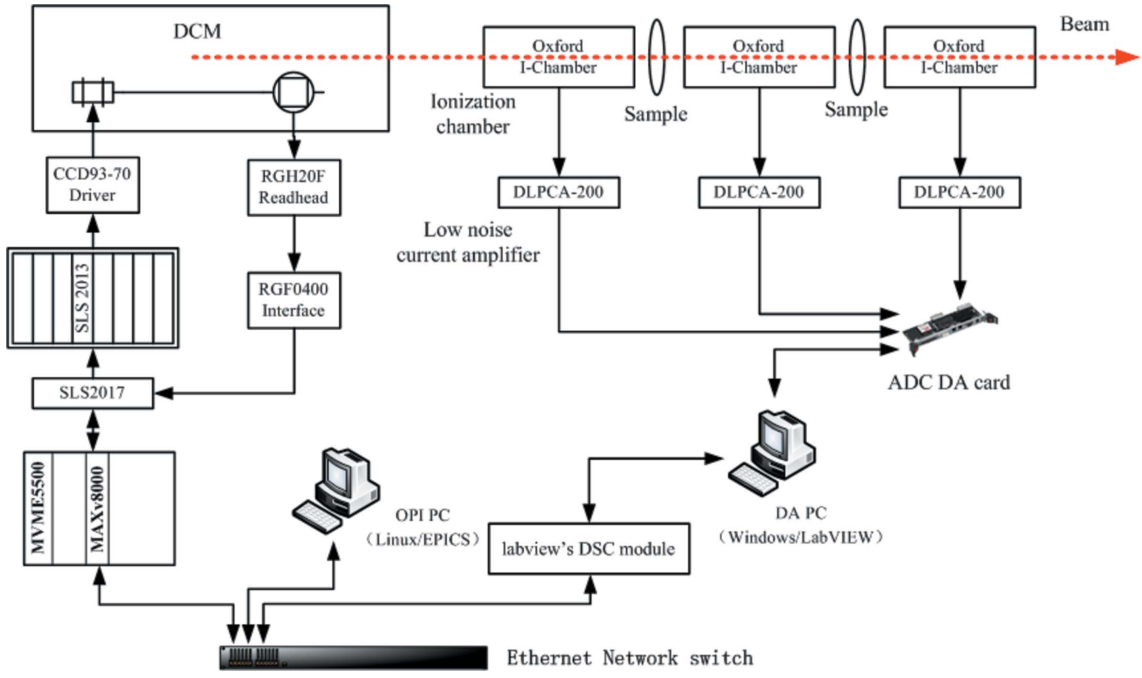

Figure 4
Schematic of the QXAFS system.

reference sample has to be measured in parallel to the sample. Further investigations will be made to solve this issue in the near future.

The DSC module is shown in Fig. 4. NI added the function that communicates with the *EPICS* system in the DSC module. The DSC module is used to design and maintain the distributed control system, complete with I/O devices (such as *LabVIEW* and OPC real-time hardware module equipment) connection. The DSC module has been tested and works well in the experiments. The control system is established by using the NI DSC module.

3. Absorption spectra

The first QXAFS spectrum at the Cu *K*-edge collected in 2 s is shown in Fig. 5. The monochromator can move continuously while acquiring increasing and decreasing spectra in hours, so there is observable dead-time. The beam current of the SSRF storage ring was operated at 3.5 GeV and 200 mA. The photon flux in BL14W1 at 10 keV could reach 10^{12} photons s^{-1} (0.1% bandwidth)$^{-1}$. In order to imitate the actual conditions in catalytic reaction experiments, the photon flux was reduced to the 10^{10} photons s^{-1} (0.1% bandwidth)$^{-1}$ level at the sample position because in a realistic catalyst the concentration of active centres is normally 5% when using the transmission mode.

Under these experimental conditions the QXAFS results are comparable with conventional XAFS. Fig. 5(*a*) shows the near-edge region of the QXAFS spectrum. The clear shoulder peak of the Cu *K*-edge indicated that the energy resolution was good enough to $2 \times 10^{-4}\,\Delta E/E$, which is lower than the design value, owing to the limited response of the ionization chambers in the QXAFS mode. Fig. 5(*b*) shows a comparison of the normalized spectra of QXAFS and conventional XAFS. Spectra in *k*-space (*k* is the wavenumber of the ejected photoelectron) and *R*-space (after Fourier transformation) of the QXAFS mode and conventional XAFS mode are presented in Figs. 5(*c*) and 5(*d*), respectively. The QXAFS spectra of Ti (Fig. 6) and Mo (Fig. 7) were also measured.

The results revealed in Figs. 5, 6 and 7 demonstrated that the QXAFS spectrum agreed very well with the conventional XAFS spectrum. The signal-to-noise ratio of the QXAFS spectrum was completely acceptable for conventional XAFS analysis.

4. Parameters optimized

Typical absorption spectra under different conditions were measured in order to optimize parameters for the QXAFS experiments. Optimizing parameters include the sampling speed of the ADC, rotation mode of the Bragg motor, height compensation of the T2 stage and number of total data points. All spectra were measured at the Cu *K*-edge with a range of 1.2 keV (pre-edge 200 eV and post-edge 1000 eV). For the comparison of the signal-to-noise ratio (S/N) under measurements with different parameters, the scan time is limited to 8 s for all set-ups. The sample was a standard copper metal foil (EXAFS Company) of thickness 3 µm. The current

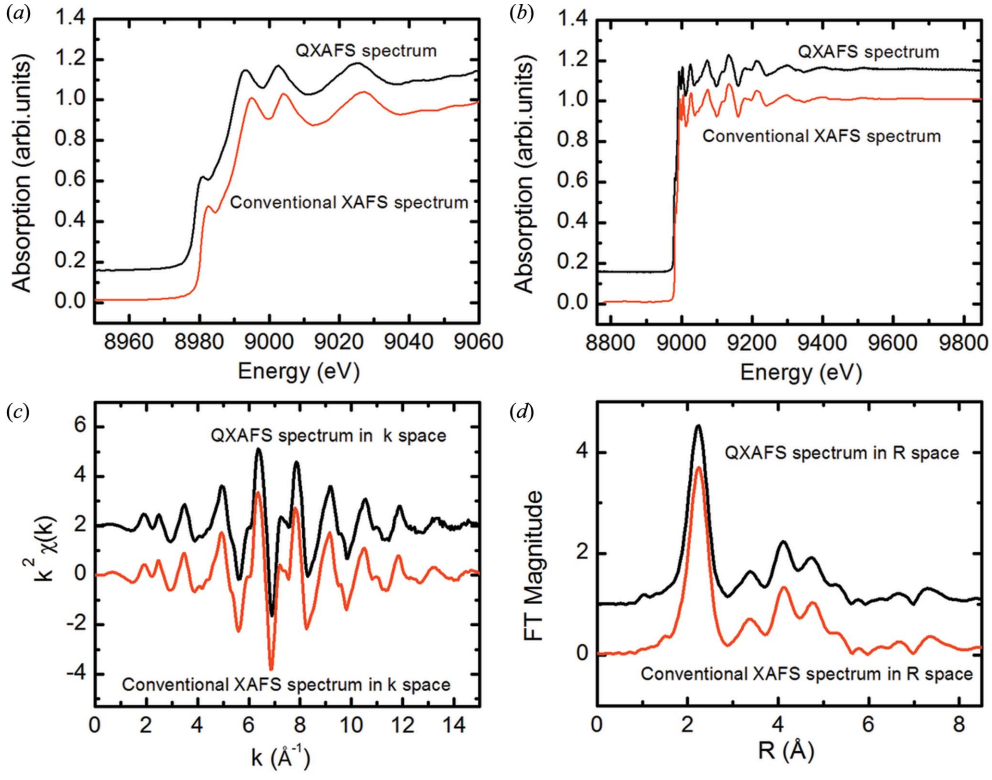

Figure 5
Comparison of the Cu *K*-edge XAFS spectra for Cu foil obtained by QXAFS measured in 2 s with a range of 1.2 keV and conventional XAFS scans: (*a*) near-edge part; (*b*) normalized XAFS spectra; (*c*) *k*-space spectra; and (*d*) *R*-space spectra.

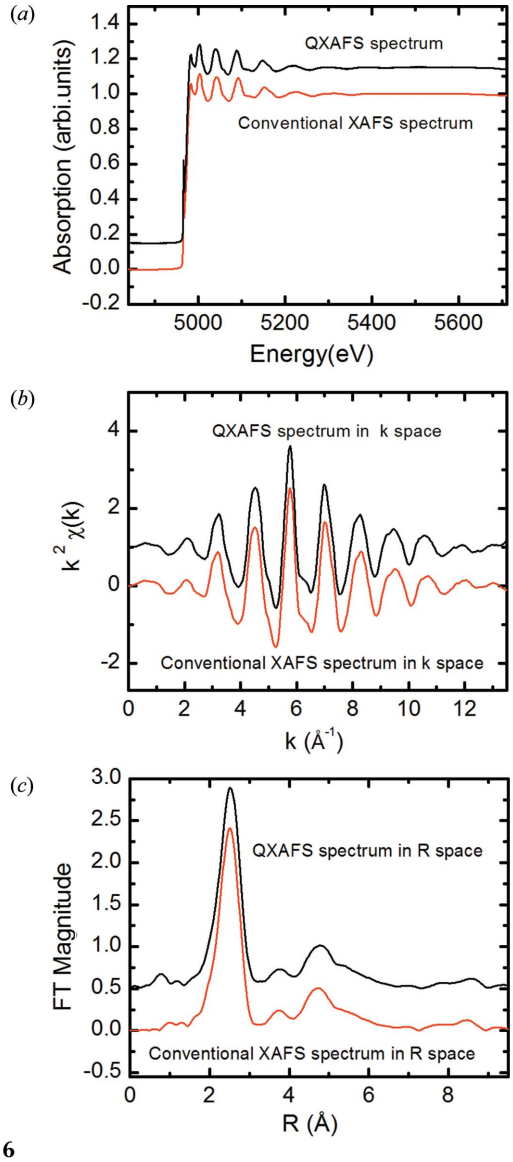

Figure 6
QXAFS spectra of Ti: (*a*) normalized QXAFS spectrum; (*b*) spectrum in *k*-space; (*c*) spectrum in *R*-space. For comparison the conventional XAFS spectra are also displayed.

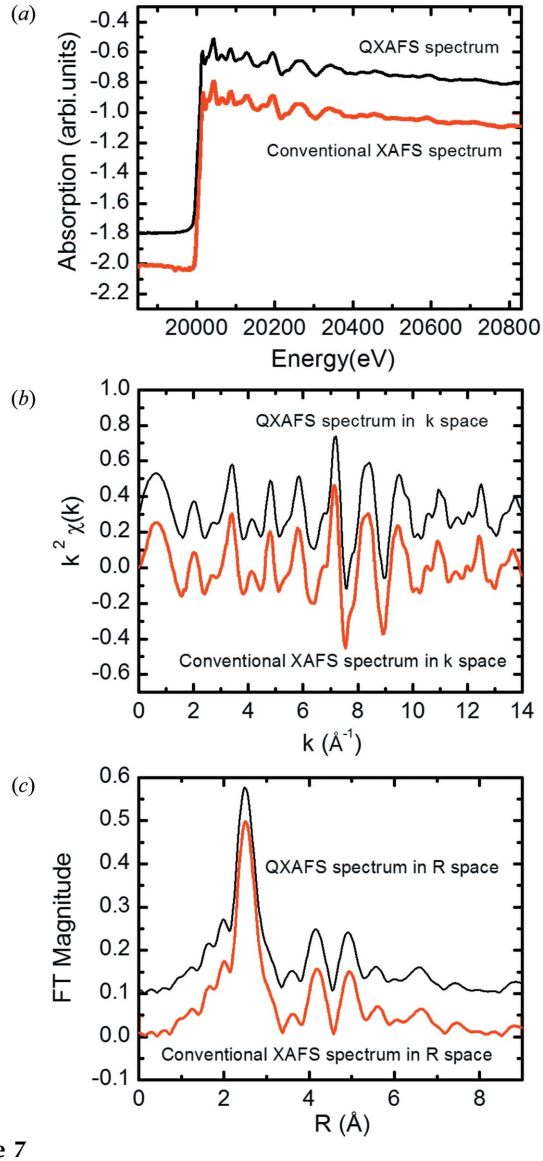

Figure 7
QXAFS spectra of Mo: (*a*) normalized QXAFS spectrum; (*b*) spectrum in *k*-space; (*c*) spectrum in *R*-space. For comparison the conventional XAFS spectra are also displayed.

amplifiers and ion chambers were set up under the same conditions with identical magnification (10^7 V A^{-1}), bandwidth mode and filling gas.

The S/N values measured under different condition are shown at Table 2. The calculation is based upon the following equation,

$$\mathrm{S/N} = 1 \Big/ \left[\sum_1^n |(I_1/I_0) - \mathrm{linearfit}(I_1/I_0)|/(I_1/I_0)\right]/n, \quad (1)$$

where n is the total number of points of the spectrum from 9800 eV to 9900 eV, which is the typical Cu standard XAFS curve, I_0 and I_1 are the currents of the first and second chamber, respectively, and linearfit(I_1/I_0) are linear fitting values based upon all of the points. Fig. 8 shows spectra which were measured at sampling speeds of 50 kHz, 100 kHz, 200 kHz, 500 kHz and 1 MHz. From the data in Table 2 it is clear that the S/N of the spectrum at higher sampling speed is higher than that at lower sampling speed. Basically the more energy points in the spectra the much higher S/N will be obtained owing to statistical fluctuation. However, when the magnification of two amplifiers was set to 10^7 V A^{-1}, the highest filter frequency was 50 kHz. With the highest filter frequency limit, the S/N is almost the same at a sampling speed of 500 kHz or higher. The reason for this is that the maximum upper cut-off frequency of the amplifier is 500 kHz. It can also be seen from Table 2 that the difference of S/N is less than 20 with sampling speeds of 500 kHz and 1 MHz. However, the buffer sometimes overflowed with a 1 MHz sampling speed, and therefore we chose 500 kHz in the normal set-up for the application of QXAFS measurements.

Stability is very important to S/N when the DCM system works in on-the-fly mode. The four spectra in Fig. 9 were measured to illustrate the stability when the Bragg motor was rotated in different modes: full-step mode, 1/2-step mode, 1/4-

Table 2
Calculated S/N under different conditions.

Error bounds (accuracies) for S/N measurement calculated using equation (1) were estimated as ±5%.

Sampling speed of ADC	Motor step	Compensation	S/N
50 kHz	1/4 step	Without	175
100 kHz	1/4 step	Without	354
200 kHz	1/4 step	Without	463
500 kHz	1/4 step	Without	677
1 MHz	1/4 step	Without	698
500 kHz	Full step	Without	338
500 kHz	1/2 step	Without	562
500 kHz	1/4 step	Without	677
500 kHz	1/20 step	Without	1284.5
500 kHz	1/20 step	With	2023

step mode and 1/20-step mode. Among the four modes the S/N of the spectrum in 1/20-step mode is higher than the others. It is shown that the S/N value of the 1/20-step mode is more than three times that of the full-step mode. Therefore we can conclude that the motor is the most stable when it runs in 1/20-step mode.

The T2 stage is very important to the fixed position of the beam on the sample, particularly for a non-uniform sample. It is necessary to consider the size of the spot because the position of the focus spot must be fixed in the experiment. The out-coming beam height will be changed by 0.1 mm without movement of the T2 stage. It is clear that there is an obvious gap between the S/N values with and without compensation (Table 2). Two of the Cu *K*-edge XAFS spectra with and without compensation are shown in Fig. 10. It is shown that the S/N of the spectrum with compensation is higher than that without compensation. This result demonstrates that it is important to keep the X-ray beam irradiating the same spot during experiments. The calculated S/N data indicate that the optimal settings for the QXAFS system at BL14W1 are a 500 kHz sampling speed for the ADC, 1/20-step mode for the Bragg motor and including the T2 stage compensation.

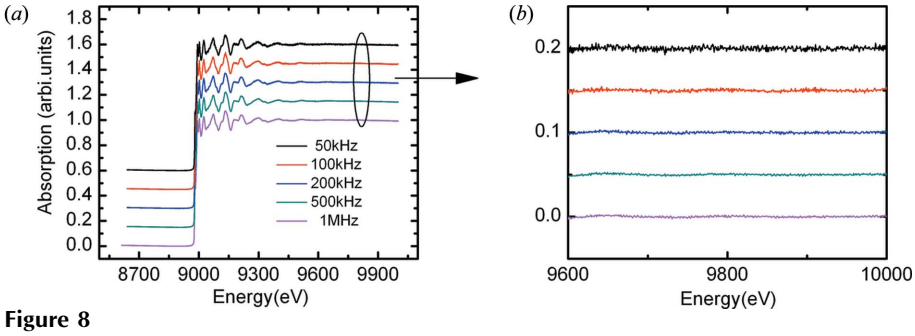

Figure 8
(*a*) Normalized XAFS spectra of the Cu *K*-edge measured at different sampling speeds (50 kHz, 100 kHz, 200 kHz, 500 kHz and 1 MHz). (*b*) Magnified plot showing the noise level at different sampling speeds (50 kHz, 100 kHz, 200 kHz, 500 kHz and 1 MHz).

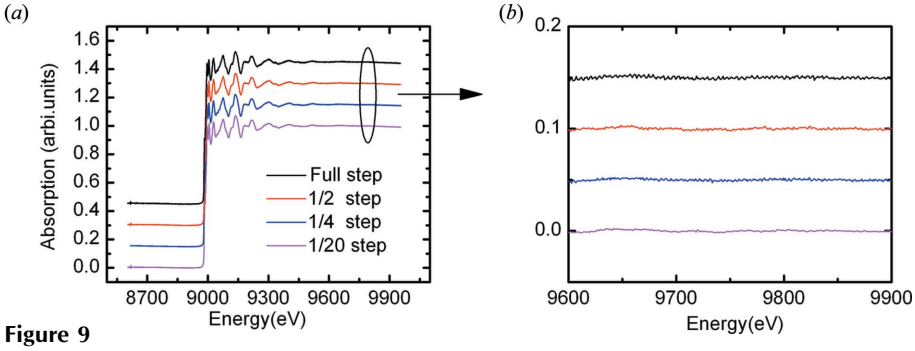

Figure 9
(*a*) Normalized XAFS spectra of the Cu *K*-edge measured at different step modes of the Bragg motor (1/20-step mode, 1/4-step mode, 1/2-step mode and full-step mode). (*b*) Magnified plot showing the noise level at different step modes of the Bragg motor (1/20-step mode, 1/4-step mode, 1/2-step mode and full-step mode).

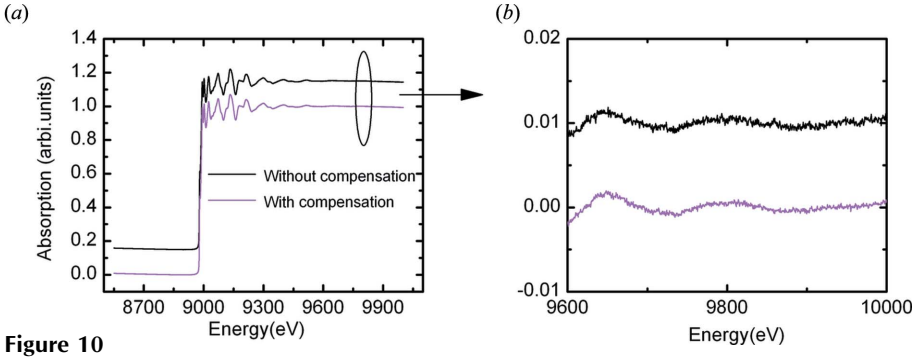

Figure 10
(*a*) Spectra of the Cu *K*-edge measured with compensation and without compensation. (*b*) Magnified plot showing the noise level measured with compensation and without compensation.

Furthermore, Fig. 11 shows the shape of the shoulder peaks which were described by a different number of points at 500 kHz sampling rate. In QXAFS mode data of one point are actually an average value over a range of energies. The resolution of the QXAFS spectrum is lower than that of the conventional XAFS spectrum when the total number of points is the same. It is important to record enough points when measuring QXAFS spectra. Contrast between different QXAFS spectra with a different number of points at the shoulder peak of the Cu *K*-edge has been carried out to ascertain the influence of the different number of points to the spectra. The shoulder peak of the Cu *K*-edge has a width of 2.5 eV. The shape of the shoulder peak with nine points is much finer than that with three points. From the contrast, it seems that 0.3 eV per point is a basic energy-step parameter for the measurement of XANES spectra at the Cu *K*-edge in QXAFS mode. This empirical value allows us to obtain a balance between the S/N and the resolution. In the future we will select a large buffer and high-sample-rate ADC to deal with this problem.

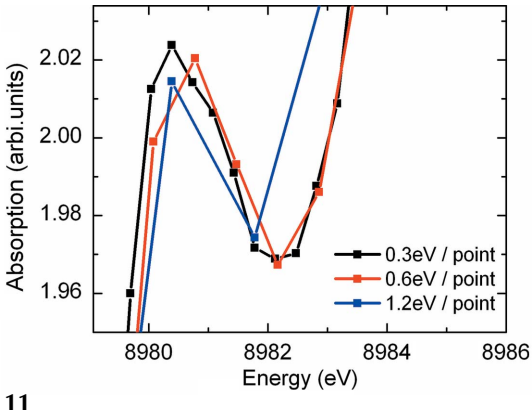

Figure 11
Shape of the shoulder peak of the Cu *K*-edge measured with a different number of points.

5. Conclusions

A QXAFS system based on *EPICS* and *LabVIEW* is achieved at the SSRF XAFS beamline. The QXAFS spectra agree very well with those collected using the step-mode XAFS method. Parameters of the QXAFS experiments were optimized *via* contrasting spectra under different conditions. The optimal parameters were set as 500 kHz ADC sampling speed, motor at 1/20 step and including the T2 stage compensation. All of the test data will provide guidance and reference for the next stage of the study: the minute-level processes both in catalysis and photo-induced reactions by X-rays will be reported based on the QXAFS method.

This work was supported by the National Natural Science Foundation of China (Grant No. 11005148, 10705046, 11135008), and the project was supported by the National Basic Research Program of China (Grant No. 2010CB934501), the Special Presidential Foundation of the Chinese Academy of Science, China (Grant No. 29) and the Science and Technology Commission of Shanghai Municipality (Grant No. 11JC1414900).

References

Beale, A. M. & Sankar, G. (2006). *Chem. Mater.* **18**, 263–272.
Beck, D., Brand, H., Karagiannis, C. & Rauth, C. (2006). *Nucl. Sci. IEEE Trans.* **53**, 930–935.
Caliebe, W. A., So, I., Lenhard, A. & Siddons, D. P. (2006). *Radiat. Phys. Chem.* **75**, 1962–1965.
Cattaneo, R., Shido, T. & Prins, R. (2001). *J. Synchrotron Rad.* **8**, 158–162.
Frahm, R. (1988). *Nucl. Instrum. Methods Phys. Res. A*, **270**, 578–581.
Frahm, R. (1989). *Rev. Sci. Instrum.* **60**, 2515–2518.
Grandjean, D., Beale, A. M., Petukhov, A. V. & Weckhuysen, B. M. (2005). *J. Am. Chem. Soc.* **127**, 14454–14465.
Hermes, S., Bremm, O., Garczarek, F., Derrien, V., Liebisch, P., Loja, P., Sebban, P., Gerwert, K. & Haumann, M. (2006). *Biochemistry*, **45**, 353–359.
Khalid, S., Caliebe, W., Siddons, P., So, I., Clay, B., Lenhard, T., Hanson, J., Wang, Q., Frenkel, A. I., Marinkovic, N., Hould, N., Ginder-Vogel, M., Landrot, G. L., Sparks, D. L. & Ganjoo, A. (2010). *Rev. Sci. Instrum.* **81**, 015105.
Liu, T., Xie, Y. N. & Hu, T. D. (2004). *Nucl. Tech.* **27**, 401–404.
Lützenkirchen-Hecht, D., Frahm, R. & Strehblow, H.-H. (1996). *J. Phys. Chem.* **100**, 10831–10833.
Lützenkirchen-Hecht, D., Grundmann, S. & Frahm, R. (2001). *J. Synchrotron Rad.* **8**, 6–9.
Newton, M. A., Dent, A. J. & Evans, J. (2002). *Chem. Soc. Rev.* **31**, 83–95.
Oudenhuijzen, M. K., Kooyman, P. J., Tappel, B., van Bokhoven, J. A. & Koningsberger, D. C. (2002). *J. Catal.* **205**, 135–146.
Pirngruber, G. D., Roy, P. K. & Weiher, N. (2004). *J. Phys. Chem. B*, **108**, 13746–13754.
Richwin, M., Zaeper, R., Lützenkirchen-Hecht, D. & Frahm, R. (2001). *J. Synchrotron Rad.* **8**, 354–356.
Stötzel, J., Lützenkirchen-Hecht, D. & Frahm, R. (2011). *J. Synchrotron Rad.* **18**, 165–175.
Uruga, T., Tanida, H., Inoue, K., Yamazaki, H. & Irie, T. (2007). *AIP Conf. Proc.* **882**, 914–916.